

Novel dual-reflection design applied for ITER core x-ray spectrometer

Cite as: *Rev. Sci. Instrum.* **93**, 073502 (2022); doi: [10.1063/5.0080718](https://doi.org/10.1063/5.0080718)

Submitted: 2 December 2021 • Accepted: 6 June 2022 •

Published Online: 5 July 2022






View Online



Export Citation



CrossMark

Zhifeng Cheng,^{1,a)}  Amro Bader,² Maarten De Bock,³ Robin Barnsley,³ Philippe Lorriere,⁴ Novimir Pablant,⁵  Fabio Costa,⁶ Joao Soeiro,⁶ Ines Bola,⁶ Martin O'Mullane,⁷ and Yevgeniy Yakusevich⁸ 

AFFILIATIONS

¹International Joint Research Laboratory of Magnetic Confinement Fusion and Plasma Physics, State Key Laboratory of Advanced Electromagnetic Engineering and Technology, School of Electrical and Electronic Engineering, Huazhong University of Science and Technology, Wuhan 430074, People's Republic of China

²Vitrociset, Via Tiburtina, 1020, 00156 Roma RM, Italy

³ITER Organization, Route de Vinon-sur-Verdon, CS 90 046, 13067 St. Paul Lez Durance Cedex, France

⁴Assystem Engineering and Operation Services SAS, 84120 Pertuis, France

⁵Princeton Plasma Physics Laboratory, Princeton, New Jersey 08540, USA

⁶Active Space Technologies S.A., 3045-508 Coimbra, Portugal

⁷Department of Physics SUPA, University of Strathclyde, Glasgow G4 ONG, United Kingdom

⁸UC Santa Barbara, Santa Barbara, California 93106, USA

^{a)}Author to whom correspondence should be addressed: chengfe@hust.edu.cn

ABSTRACT

A novel dual-reflection configuration is introduced for the International Tokamak Experimental Reactor (ITER) core x-ray spectrometer to fit the allocated space where it will be placed accompanied by moving the detectors backward to reduce the incident radiation dose. The highly oriented pyrolytic graphite, which has a mosaic structure of microscopic crystallites, is chosen for the front reflector motivated by higher x-ray throughput and stronger misalignment tolerance compared to the perfect crystal reflector. In the ITER core x-ray spectrometer, a combination of several reflector-deflected Lines of Sight (LOSs) and a direct LOS is proposed for the first time named X-Ray Crystal Spectroscopy Core (XRCS-Core). The system is optimized to observe lines from externally seeded xenon and the intrinsic tungsten impurity, meeting both port integration needs and measurement requirements. Its spectral performance is simulated using an analytical-raytracing mixed code—XRSA, showing good imaging quality with a spectral resolution higher than 8000. The XRCS-Core system is thought to be applicable in various ITER scenarios through the assessment taking into account the spectrometers' specifications and the chosen lines' emissivity in different plasma parameters.

Published under an exclusive license by AIP Publishing. <https://doi.org/10.1063/5.0080718>

I. INTRODUCTION

The core x-ray spectrometer in the International Tokamak Experimental Reactor (ITER) is dedicated to providing the profiles of the ion temperature and plasma rotation in the core plasma region.^{1–3} In the past decades, several concepts were proposed for this diagnostic. The early designs envisioned covering the ITER plasma with multiple lines of sight from multiple spectrometers.^{2–4} Along with the maturation of the x-ray imaging spectrometer supported by the development of the x-ray imaging detector,^{5,6} the

last design was simplified by adopting a spherically bent crystal to both disperse and image x rays emitted from the plasma onto a two-dimensional detector.^{7,8} Thus, the diagnostic was named Core Imaging X-ray Spectrometer (CIXS).

The CIXS was located at equatorial port 17, as shown in Fig. 1. Its concept was based on direct imaging of three views (lower, middle, and upper) in a dominantly poloidal plasma cross section with a small toroidal angle to allow for toroidal rotation measurements directly imaged by three analyzing crystals on detectors just behind (2, middle and lower views) and inside

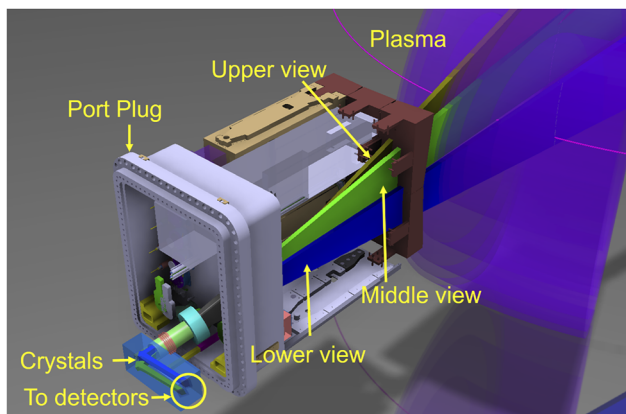


FIG. 1. Original configuration of ITER CIXS in equatorial port 17 with three views predominantly in the poloidal.

(1, upper view) the Port Plug (PP) in a Johann spectrometer configuration.

The imaging configuration, together with the required poloidal coverage, resulted in the spectral dispersion plane in the toroidal direction. This meant that the detectors were very close to the PP closure plate, having the advantage that only very short vacuum extensions were needed and no components needed to be installed on the Interspace Support Structure (ISS). On the other hand, it was accompanied by a more complex integration and the high radiation levels at the detector location (neutron flux $>1 \times 10^8 \text{ n s}^{-1} \text{ cm}^{-2}$ in D-T operation), leading to radiation-induced noise and likely multiple detector replacements during the ITER lifetime.⁹

However, due to a reconfiguration of the Disruption Mitigation System (DMS) locations in ITER, the core x-ray spectrometer system has now moved to equatorial port 2, which imposes different boundary conditions on the arrangement of this diagnostic. The

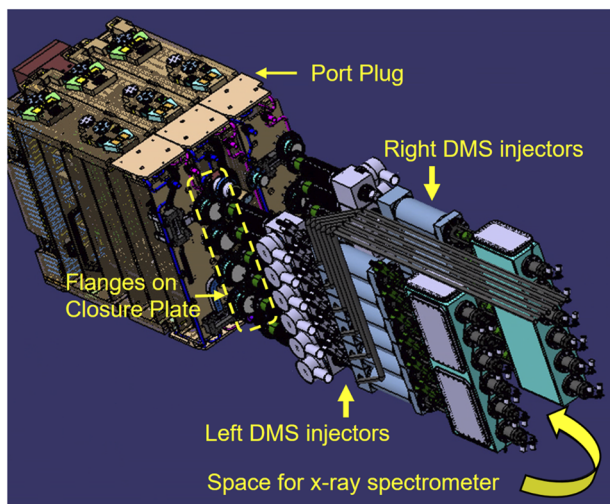


FIG. 2. Equatorial port 2 integration environment with the two sets of DMS injectors to either side and the space reservation for the core x-ray spectrometer system.

biggest impact is that the neighboring DMS pellet injectors in equatorial port 2 require straight injection paths through both the PP and ISS. This means that the diagnostic is sandwiched between the DMS injectors and the spectral dispersion plane in the toroidal direction compared to the equatorial port 17 case is no longer possible (see Fig. 2).

This paper will introduce a novel design with a dual-reflection scheme, where the analyzing crystal and detector are placed at the back end of the ISS after the Bioshield. All components are distributed in a narrow space fitting the allocated envelope with a vertical spectral dispersion plane. In addition, the system performance and its applicability in various ITER scenarios are also discussed.

II. DUAL-REFLECTION SCHEME AND THE NOVEL DESIGN

The dual-reflection concept was introduced for ITER-98 using an array of front graphite reflectors near the plasma to view a wide range of minor radii each with a toroidal component.^{2,4} Each reflector was assigned to one crystal spectrometer at the backside after the shield with the expectation of a large reduction in the neutron flux at the spectrometer side. To sufficiently cover the ITER plasma, 16 lines of sight (correspondingly, 16 spectrometers) were proposed. Nevertheless, these numerous spectrometers would considerably complicate the system integration, which is not compatible with the present allocated space either.

The novel design adopts an idea combining the front reflector configuration and Johann imaging scheme. As shown in Fig. 3, this concept is composed of several front reflectors and a spectrometer, including one spherical analyzing crystal and one detector. Taking into account the toroidally narrow but poloidally ample space in equatorial port 2, the spectrometer's meridional plane (diffraction plane) is set in the vertical direction. Thus, the arm between the crystal and detector is vertically configured with the possibility to achieve a relatively long meridional focus providing a higher spectral resolution. The reflector is made of Highly Oriented Pyrolytic Graphite (HOPG), which has a mosaic structure of microscopic crystallites with a narrow distribution in orientation angles.¹⁰ This gives HOPG a reduced peak reflectivity but a much wider wavelength band, leading to a significantly higher integral reflectivity

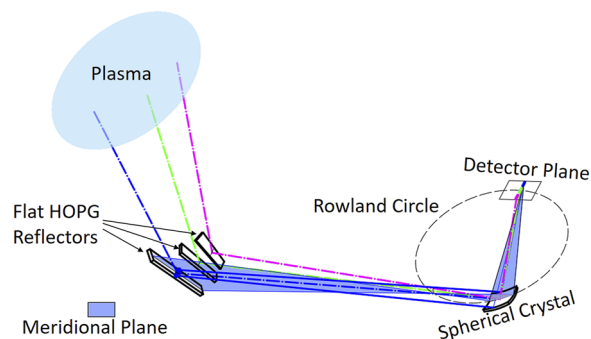


FIG. 3. Concept of the dual-reflection x-ray spectrometer with multiple front reflectors.

(typically, more than 20 times higher) than the pure crystals. In the dual-reflection design, the reflectors are flat and specifically oriented to view the desired regions in the plasma and distributed in the spectrometer’s sagittal plane (spatial resolving plane) with enough gap making the spectrometer able to identify each reflector’s image. Given that this modified design is no longer an imaging system, the name of this diagnostic is changed to X-Ray Crystal Spectroscopy Core (XRCS-Core).

The x-ray Bragg reflection is constrained by the extremely narrow wavelength band, which raised the requirement of the precise orientation of the reflectors and analyzing crystal to fit the Bragg angle at a certain wavelength. This, in turn, means the emission lines of interest and the impurities that emit them have to be chosen early on and cannot be changed later without a complete redesign of the diagnostic system layout.

Several candidate impurities—e.g., tungsten (W), iron (Fe), argon (Ar), krypton (Kr), and xenon (Xe)—had been investigated to estimate the applicability of the previous designs.^{4,7,11} Although the intrinsic impurities (W and ion Fe) show the applicability in certain operation scenarios, the potential of their low concentration in the ITER plasma and the non-adjustability would lead to a risk to the measurement access. As for the present design with the additional reflector, the choice of the impurity lines is a balance between the emissivity over multiple plasma scenarios, the Bragg angles on the front reflectors and analyzing crystals and the efficiency of reflection and detection. After a series of comparisons, the lines from Xe ions show greater achievability for the full spatial coverage (via the deflection of front reflectors) and higher overall efficiency than the previously proposed lines from Kr³⁴⁺ and Kr³⁵⁺. The final selected impurities are the intrinsically available tungsten for the emission line (1.3596 Å $2s^2 2p^6 1S_0 - 2s^2 2p^5 ({}^2P^{\circ}_{3/2}) 3d ({}^3/2, {}^5/2) {}^{\circ} 1$) from W⁶⁴⁺ in the plasma core, plus extrinsically seeded xenon for the emission line (2.1899 Å $2s^2 S_{1/2} - 3p^2 P^{\circ}_{3/2}$) from Xe⁵¹⁺ in the plasma core and the line (2.7203 Å $2p^6 1S_0 - 2p^5 {}_{3/2} 3d_{5/2} ({}^3/2, {}^5/2) {}^{\circ} 1$) from Xe⁴⁴⁺ more toward the plasma edge.

The crystal directions should be selected to have the Bragg angle near 50°, taking into account that the spectrometer should identify the reflectors determined by the sagittal focusing. Here, germanium crystals are chosen as the material for analyzing crystals with the Bragg angle of ~50° for the three selected lines. Due to the relatively wide bandwidth (compared to Si and quartz), the germanium crystal leads to higher efficiency. Table I lists the reflection properties of the selected materials, where θ_{Bragg} represents the Bragg angle; R_p and Full Width at Half Maximum (FWHM) denote the peak reflectivity and the effective width, respectively, according to the rocking curve obtained from XOP.¹² The Bragg angles for W⁶⁴⁺ and Xe⁵¹⁺ lines are both less than 20°, appropriate for deflecting LOSs from the central plasma region; the Bragg angle for the Xe⁴⁴⁺ line is reasonably larger, suitable for deflecting light from the approaching edge region.

As depicted in Fig. 4, the XRCS-Core is divided into five subviews; each view, except the middle one (green view), has four lines of sight (LOSs) for which three (two for green view) LOSs are deflected by front reflectors in the PP, respectively, and the remaining LOS is the direct viewing channel. All four LOSs (three for green view) eventually arrive at the same analyzing crystal in the rear part of ISS. As for the five subviews, two are dedicated to measuring the Xe⁵¹⁺ line in the inner region (0–0.55a, where “a” denotes the minor

TABLE I. Reflection properties of selected materials for corresponding emission lines.

Lines	Reflector reflection [0.4° HOPG (0 0 2)]		Crystal reflection	
	θ_{Bragg} (deg)	R_p / FWHM	θ_{Bragg} / Crystal indices	R_p / FWHM
Xe ⁴⁴⁺ 2.7203 Å	23.97	0.31 8765 μ rad	52.88 Ge (1 1 3)	0.78 90.3 μ rad
Xe ⁵¹⁺ 2.1899 Å	19.05	0.34 8990 μ rad	50.6 Ge (0 0 4)	0.93 71.7 μ rad
W ⁶⁴⁺ 1.3596 Å	11.72	0.42 9597 μ rad	51.99 Ge (3 3 5)	0.86 11.4 μ rad

radius); two are dedicated to measuring the Xe⁴⁴⁺ line in the outer region (0.5–0.85a), which is expanded to ~0.2a with the direct LOS; the last subview is dedicated to measuring the W⁶⁴⁺ line foreseen available at the core.

The curvature of the crystal is determined to make the sagittal focus (object side) close to the reflectors with the curvature radius of ~2.2 m. The distance of the meridional focus to the crystal is ~1.8 m, which is compatible with the space envelope for integrating the detectors, providing a relatively high spectral dispersion beneficial for achieving a good spectral resolution. The crystal size is constrained by the integration of the five crystals and the sight cones from multiple front reflectors. Thus, the same size of 40 mm width (in spectral diffraction direction) by 50 mm height (in spatial resolving direction) is applied to all crystals.

Taking into account the need to identify the reflector image, the cross section of the sight cone approaching the reflector is constrained to be rectangular with the same size for the individual subviews. The cross section size is 40 mm (in spectral diffraction direction) by 30–35 mm (in spatial resolving direction) to match the latter vacuum pipe diameter. Given the sight cone shape is controlled by the effective reflector surface, the surface shape varies to match the footprint cutting the sight cone due to the customized orientation for each reflector.

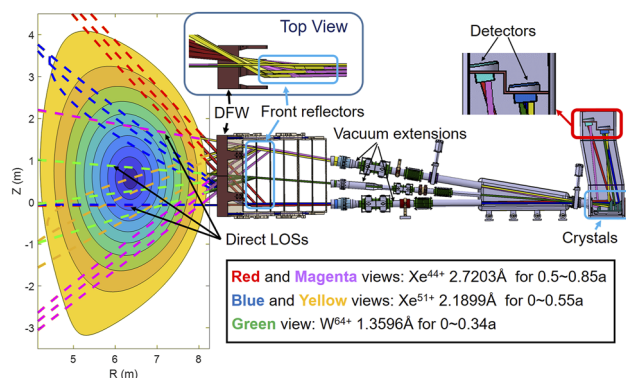


FIG. 4. XRCS-Core layout with five dual-reflection subviews.

The aperture of the direct viewing channel is controlled by the slit on the Diagnostic First Wall (DFW) with the size of 40 mm (in spectral diffraction direction) by 20 mm (in spatial resolving direction), which provides flexibility for the spectrometer. It can expand the viewing range and keep working in case the front reflector fails. In terms of the rotation measurement, the toroidal fraction is ignorable for the direct viewing channel. The poloidal velocity is commonly much lower than toroidal velocity, and it is the same for the predicted ITER plasma rotation. Thus, the direct viewing LOS could be used as the reference channel in terms of the toroidal rotation measurement without the need for the strict wavelength calibration.

Considerable efforts are made to optimize the system integration. For instance, five subviews are grouped such that only three vacuum extension pipes are needed outside the PP; at the back end, the LOSs are regrouped so that only two detector heads (Multi-module PILATUS-3 detectors) are needed. Also, the sightlines are oriented such that they converge inside the DFW to ensure the smallest possible cut-out in the DFW. This is necessary to maximize neutron shielding and ensure the manufacturability of the DFW cooling channels and to ensure enough structural integrity of the DFW. Then, the front reflectors are positioned in the (toroidal) center of the Diagnostic Shield Module (DSM) and oriented such that the different LOSs follow nearly overlapping paths. Again this allows for minimizing the cut-outs, maximizing neutron shielding, and enhancing the structural integrity of the DSM.

III. SYSTEM PERFORMANCE ASSESSMENT

To systematically assess the dual-reflection x-ray system, an analytical-raytracing mixed code XRSA (X-Ray Spectroscopy Analysis) is developed. Figure 5 characterizes the strategy applied in this code, where the main point is to generate the rays by connecting the uniformly meshed grids on the source and the first x-ray optic (reflector in this case). The contribution of each ray to the signal intensity on the detector is carried by a specific term,

$$\Delta I = \Delta E \cdot \Delta \Omega \cdot k_R \cdot k_C, \quad (1)$$

where ΔE denotes the emission power from the x-ray source cell; $\Delta \Omega = \Delta S/(4\pi d^2)$ denotes the effective solid angle (ΔS represents the projection area of the reflector grid, and d is the distance between

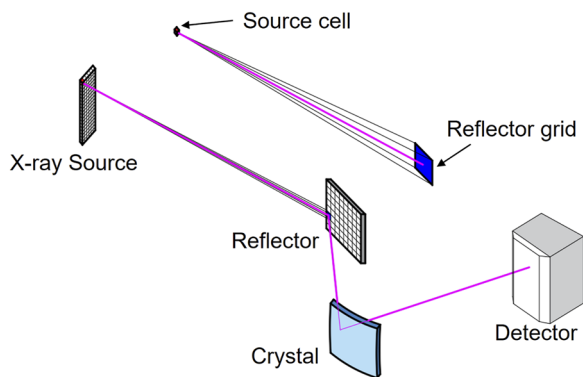


FIG. 5. Schematic diagram of the XRSA code.

the source and reflector units); k_R represents the reflector reflectivity, which is calculated according to the ray's incidence angle on the reflector and the reflector's rocking curve for the applied x-ray wavelength; k_C represents the crystal reflectivity deduced according to the ray's incidence angle on the crystal and the crystal's rocking curve for the applied x-ray wavelength.

Following this strategy, the XRSA code can be flexibly utilized to evaluate the performance of the dual-reflection x-ray spectral system and simulate the acquired spectral diagrams with a reduced ray amount. The code's accuracy is verified via comparison with the full ray-tracing code XICSRT.¹³ Figure 6 presents the simulated image, based on the pixel size ($0.172 \times 0.172 \text{ mm}^2$) of PILATUS-3, from the x-ray source with nine uniformly distributed monochromatic wavelengths, to test the system imaging and efficiency, where the x-axis is the spectral diffraction direction and the y-axis is the spatial resolving direction. The wavelength interval is 0.005 \AA for Xe^{44+} and Xe^{51+} spectrometers and 0.003 \AA for W^{64+} spectrometers. It could be seen that different channels are clearly distinguished, shown as vertically separated spots on the detector plane. The spot color is in line with the LOSs' color in Fig. 4, representing the image from the corresponding subview.

Under the dual-reflection design, the spectral resolution is determined by the analyzing crystal. Due to the long focal length and the relative short objective (reflector), the imaging bending is ignorable for each channel, resulting in ideal imaging on the detector plane. For the Xe^{44+} and Xe^{51+} spectrometers, the image width is somewhat affected by the wide rocking curve of the germanium crystal, having the FWHM ~ 1.5 pixels with full channel vertical binning. The spectral dispersion is $\sim 1.8 \times 10^{-4} \text{ \AA/pixel}$ for all Xe^{44+} and Xe^{51+} spectrometers; thus, the spectral resolution is estimated as $\sim 2.7 \times 10^{-4} \text{ \AA}$ ($\lambda/\Delta\lambda > 8000$ for Xe^{51+} spectrometer and $\lambda/\Delta\lambda > 9000$ for Xe^{44+} spectrometer). For the W^{64+} spectrometer, FWHM is found to be less than the pixel width with the narrower rocking curve. Thus, its spectral resolution is predominately limited by the pixel size. With the spectral dispersion $\sim 1.06 \times 10^{-4} \text{ \AA/pixel}$, it achieves a relative resolution of $\lambda/\Delta\lambda > 10\,000$.

The effective etendue could be evaluated according to the overall intensity of each channel from a normalized x-ray source. It combines the etendue constrained by the optical aperture and the attenuation factors from reflections on the front reflector and crystal. Figure 7 presents the simulated effective etendue at different wavelengths. For all Xe spectrometers, the etendue of the straight channel from the direct LOS is 1.5–2 times that with reflectors; the bandwidths, evaluated from the FWHM of the effective etendue diagrams, are both estimated as 0.032 \AA for the Xe^{44+} spectrometers

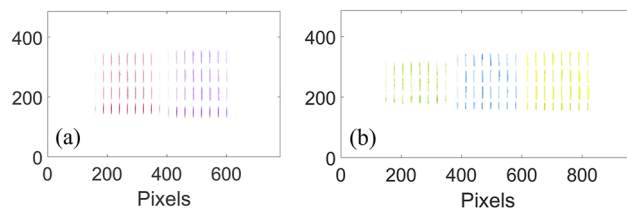


FIG. 6. Image on detectors from the x-ray source with nine uniformly distributed wavelengths. (a) Images from two Xe^{44+} spectrometers and (b) images from two Xe^{51+} spectrometers and W^{64+} spectrometer.

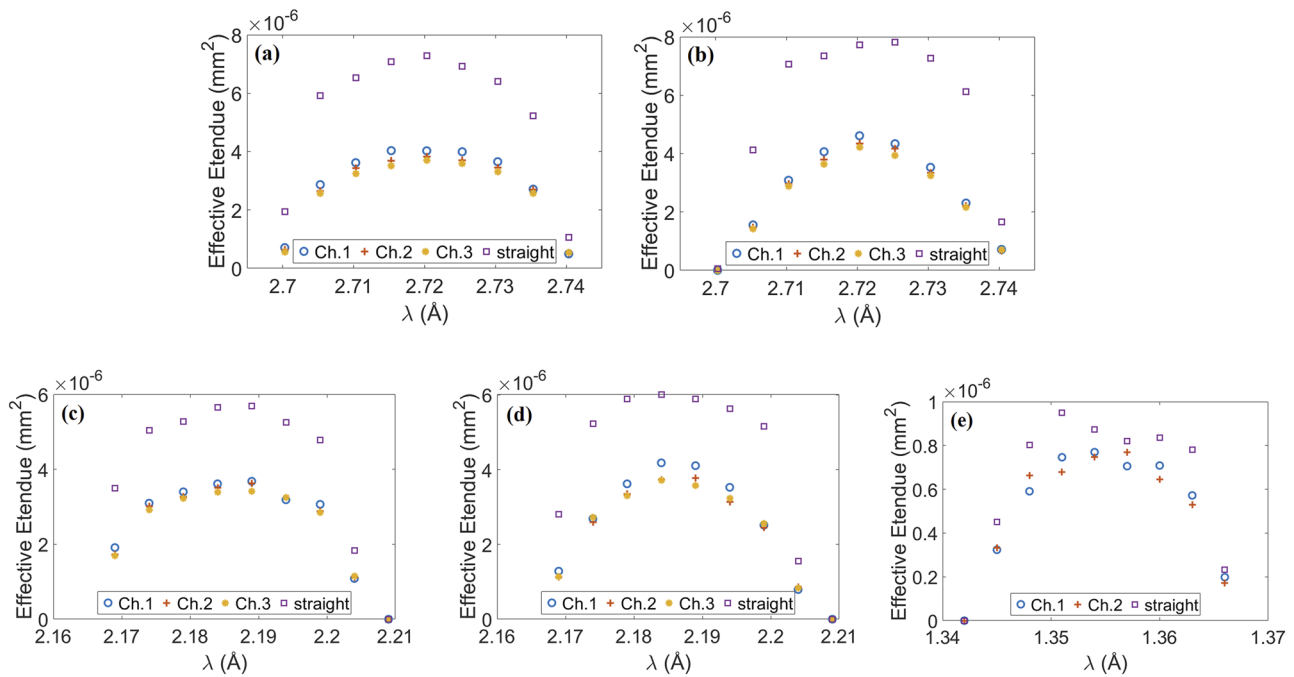


FIG. 7. Effective etendue at different wavelengths for (a) Xe^{44+} spectrometer (red sight), (b) Xe^{44+} spectrometer (magenta sight), (c) Xe^{51+} spectrometer (blue sight), (d) Xe^{51+} spectrometer (yellow sight), and (e) W^{64+} spectrometer (green sight). A “straight” channel corresponds to the lowest row in Fig. 6; “Ch.1” to “Ch.3” correspond to row 2 to row 4 in Fig. 6 (counted from the lower side).

(red and magenta LOSs) and 0.031 \AA for the Xe^{51+} spectrometers (yellow and blue LOSs) with or without the reflectors. This means that the system’s bandwidth is not quite limited by the reflector’s rocking curve but is dominated by the aperture size. For the W^{64+} spectrometer, the effective etendue is somewhat lower with the bandwidth of $\sim 0.02 \text{ \AA}$ due to the narrower rocking curve for the crystal at the shorter wavelength.

IV. APPLICABILITY IN ITER SCENARIOS AND DISCUSSION

A. XRCS-core applicability in ITER scenarios

The XRCS-core is foreseen to be equipped starting from ITER Pre-Fusion Power Operation Phase (PFPO-1) with multiple plasma

operations. As a passive spectrometer, the XRCS-Core’s applicability depends on the Xe ion concentration in the desired ionization state in the corresponding LOS. The electron temperature in ITER is foreseen to vary from $\sim 1 \text{ keV}$ up to 30 keV , which dramatically affects the impurity’s charge state distribution in the plasma. There are very few Xe experimental spectral data in the tokamak. Here, we utilize the FLYCHK¹⁴ database benchmarked with ADAS¹⁵ data to evaluate the Xe lines emissivity in the ITER plasma.

In this paper, we choose an L-mode $I_p = 5 \text{ MA}$ scenario and an H-mode $I_p = 15 \text{ MA}$ scenario from the ITER Integrated Modeling and Analysis Suite (IMAS) database to assess the diagnostic’s applicability, as presented in Fig. 8 with the plasma parameters’ profiles. Since tungsten is uncontrollable in the ITER plasma as the intrinsic impurity, only xenon is used for the following assessment. To simplify the procedure and adapt to general scenarios,

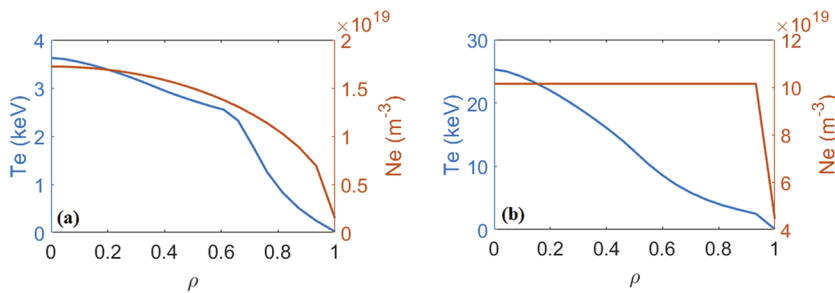


FIG. 8. Electron temperature and density profiles for diagnostic’s applicability assessment. (a) L-mode $I_p = 5 \text{ MA}$ scenario [Integrated Modeling and Analysis Suite (IMAS) shot: 100 013] and (b) H-mode $I_p = 15 \text{ MA}$ scenario (IMAS shot: 130 011).

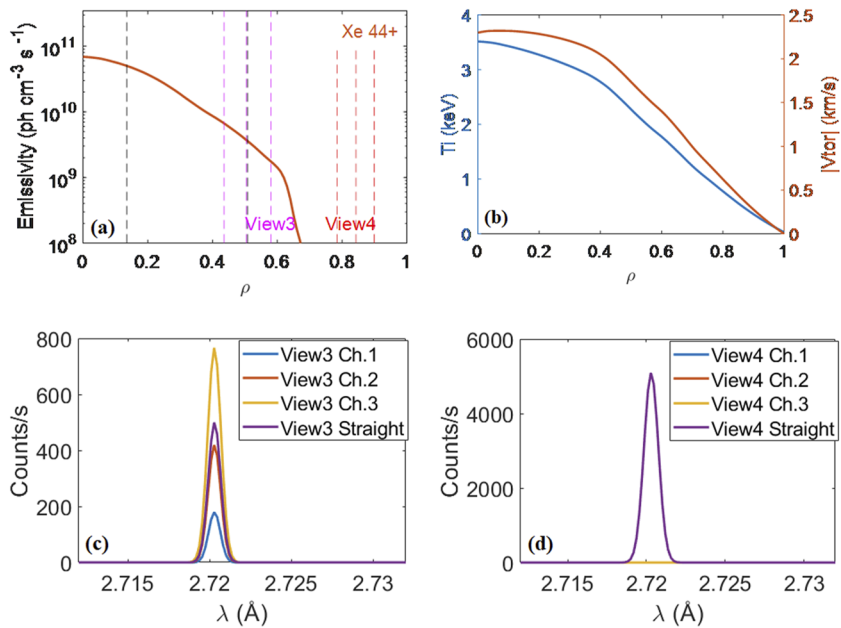


FIG. 9. (a) Xe line emissivity profile (vertical dashed lines represent the LOSs' tangent positions to the flux surfaces, color in line with the definition in Fig. 4 with the black dashed line representing the straight LOSs), (b) ion temperature and plasma rotation profiles, (c) and (d) simulated spectra for multiple channels for the L-mode $I_p = 5$ MA scenario.

here we only apply a uniform relative Xe concentration for the assessment.

The Xe lines emissivity profiles evaluated with FLYCHK atomic data in the two cases are presented in Figs. 9(a) and 10(a), where the

Xe concentration is determined by constraining the additional radiation power as 1 MW in the bulk plasma. For the L-mode $I_p = 5$ MA scenario, the Xe concentration is 3.94×10^{-4} relative to the electron density; for the H-mode $I_p = 15$ MA scenario, the Xe concentration

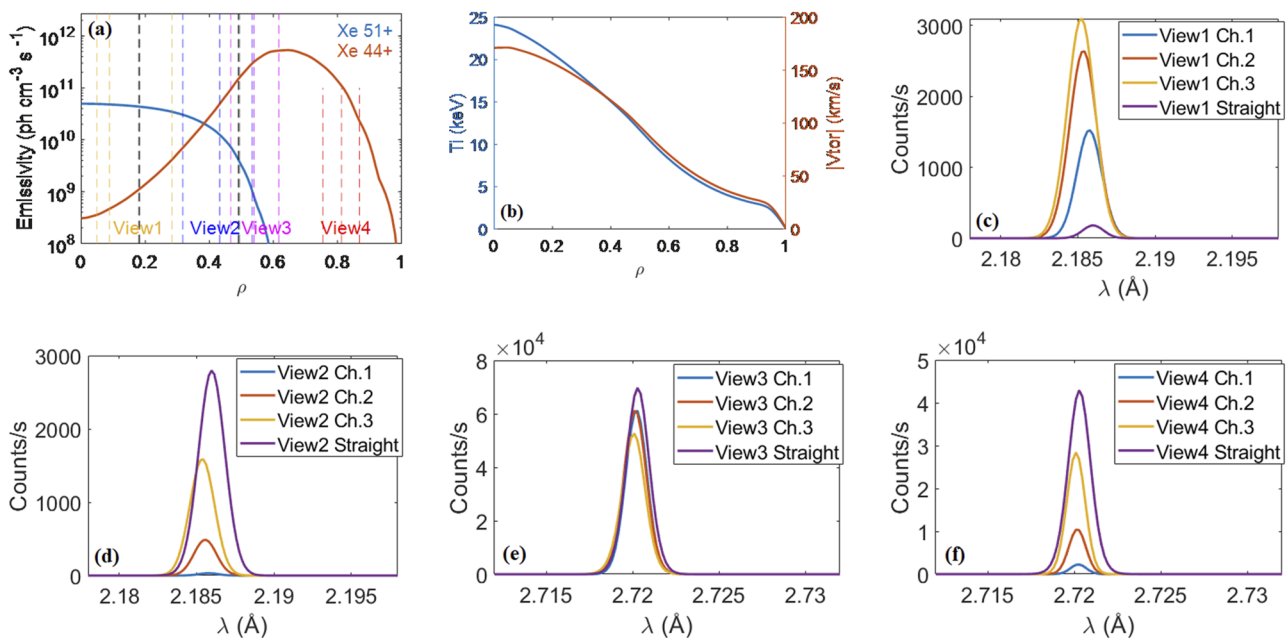


FIG. 10. (a) Xe lines emissivity profiles (vertical dashed lines represent the LOSs' tangent positions to the flux surfaces, color in line with the definition in Fig. 4 with the black dashed line representing the straight LOSs), (b) ion temperature and plasma rotation profiles, and (c)–(f) simulated spectra for multiple channels for the H-mode $I_p = 15$ MA scenario.

is 1.23×10^{-5} relative to the electron density. It could be seen that only the Xe^{44+} line is available at the central region in the L-mode scenario, where the central electron temperature is 3.6 keV. In the H-mode scenario with the central electron temperature of 25 keV, Xe^{51+} concentrates in the core, and Xe^{44+} peaked at the outer region ($\rho \sim 0.7$). The vertical dashed lines denote the LOSs' position in the plasma, taking into account the flux map for each case from IMAS.

The spectra, as shown in Figs. 9(c) and Figs. 9(d) and Figs. 10(c)–Figs. 10(f), are simulated using an analytic method aided by the numeric approach, taking into account the ion temperature and toroidal rotation profiles [Figs. 9(b) and 10(b)] from IMAS data. Here, the LOS in plasma is divided into multiple equal subintervals, where the local line emissivity contributing to the spectral intensity, the local ion temperature contributing to the spectral width, and the local plasma rotation contributing to the wavelength shift are taken into account to generate the subspectra. Then, the spectral diagram is deduced by summing up the subspectra for each LOS according to the line dispersion and the pixel size of the PILATUS detector. To simplify the process, the instrumental profile is set to be Gaussian-shaped with $\lambda/\Delta\lambda = 8000$, and only Doppler broadening and shift are applied for integration along with the LOSs. The presented count rates are the total values by summing the counts along the vertical pixels for each channel.

It could be concluded that the Xe^{44+} spectrometers can provide a few available channels in low plasma parameter cases with the strongest one from the direct LOS most toward the center. With the high core electron temperature (>20 keV), the XRCS-core can achieve a relatively full viewing coverage by combining Xe^{51+} and Xe^{44+} spectrometers.

The LOSs in the plasma are distributed discretely over the upper and lower space, which is made to fit the integration of all subviews. This may lead to some difficulty in data analysis. Similar to the cases with the plasma axis offset, the distribution of these LOSs would become non-uniform, which would make the evaluation of ion temperature and plasma rotation profiles more complicated. On the other hand, this would be beneficial in some aspects. As for the straight sights with the ignorable toroidal component, the two-side allocation makes them available for poloidal rotation evaluation, and then these straight sights would be more perfectly suitable as the reference for toroidal rotation evaluation. From the spectra in Figs. 10(c)–10(f), we can clearly observe the wavelength shifting due to the toroidal rotation. The exact shifting value could be calculated by fitting the data. Thus, with the reference wavelength from the straight sight, we could obtain the absolute rotation velocity.

B. Discussion on the role of the front reflector

With the introduction of the front reflector, the x-ray spectrometer is much more flexible in terms of the system's layout, allowing the movement of x-ray detectors at the back of the ISS just behind the Bioshield. Although the system efficiency is reduced by 70% (compared to the original layout without reflectors under the same aperture) due to the relatively low peak reflectivity (R_p) of HOPG, it is largely compensated by the fact that the radiation-induced noise is strongly suppressed. The neutron rate behind Bioshield is estimated to be $\sim 10^6/\text{cm}^2 \text{ s}$ in the ITER D-T operation, which is much more beneficial for the detector's survival.

The reflector's efficiency is determined by effective reflectivity. The perfect crystal usually has a peak reflectivity up to 90%, but its narrow bandwidth extremely limits the filling area on the crystal, which actually causes an unacceptable low efficiency for most ITER scenarios. The mosaic crystal achieves a much wider reflection band, despite somewhat reduced peak reflectivity, which still provides higher integral reflection efficiency. Furthermore, its tolerance for the misalignment from assembly and thermal expansion is increased with the wide reflection bandwidth, which by far is compatible with ITER operational environment according to ongoing engineering analysis. Still, the alignment between the reflector and crystal is foreseen to be a challenge, and thus, a dedicated on-situ alignment device is needed.

C. Noise and uncertainty

As the detector is moved behind the Bioshield with foreseen a relatively low neutron flux, the neutron-induced count rate is expected as less than 10^3 counts/cm² s by assuming the neutron sensitivity of 10^{-3} counts/n, resulting in ~ 10 counts/s pixel with binning on all vertical pixels for each LOS.

The most significant noise for the system would be the statistic Poisson noise, which is proportional to the square root of the number of counts. It may reduce the Signal-to-Noise Ratio (SNR) specifically for the Xe^{51+} signals, due to its relatively low emissivity and the strong continuum of Bremsstrahlung radiation at the core region. Unlike the existing tokamaks, the continuum emission from Bremsstrahlung is of the same order or larger than the line emission at core ITER plasma due to the high electron temperature and density. It adds extra Poisson statistic fluctuation on the spectrum for the Xe^{51+} signal, as the continuum background will be subtracted for the further spectrum fitting. According to the spectral diagrams at the inner region in Figs. 10(c) and 10(d) (here, the continuum emission is not included), the statistic Poisson noise shall significantly constrain the time resolution assuming that the continuum level is at the same level as the line peak. In this case, the average SNR for the central channel is ~ 25 with 1 s exposure and ~ 8 with 100 ms exposure. The SNR can be improved by adding more Xe to the core (if the higher additional radiation loss is acceptable). In the edge region or other cases with lower electron temperature, Xe^{44+} can always provide good signals supporting the measurement.

The neutron sensitivity is referred to the experimental results on JET, where an effective attenuation factor of 10^6 is observed on the multiwire proportional counter.⁴ However, there is no relevant data for the Hybrid Photon Counting (HPC) detector applied to the PILATUS detector by far. The specific test is planned to be carried out in the near future.

For ITER plasmas, there is no robust theory of impurity transport that can predict all phases. The radial convection velocity is foreseen to be outward-directed due to the high pedestal temperature and the high separatrix density in the H-mode plasma.¹⁶ In addition, the inward impurity drift decreases with the decreasing plasma density gradient.¹⁷ Thus, according to the typically desired flat density profile in the ITER plasma, impurity will be highly screened, achieving a hollow profile. This may lead to high edge Xe accumulation radiating a large fraction of the power at the boundary region but with very low Xe density in the core. On the other hand,

the impurity can penetrate through the edge transport barrier due to ELM mixing in the ELM-H-mode.¹⁸

The Xe atomic data are also needed to be explored specifically in the high-temperature plasma. The Xe⁴⁴⁺ line has been observed in the tokamak plasma, with few attempts of Xe injection experiments.^{19,20} The experimental results in the C-Mod tokamak plasma show good agreement with the calculations from the SCRAM code in the vicinity of the 3D transition. However, the electron temperature in the present tokamak is too low to generate the highly charged Xe⁵¹⁺ ion. The atomic data, such as the line wavelength and the photon emissivity coefficient, are not fully demonstrated.

V. SUMMARY

A novel dual-reflection configuration with several discrete channels deflected by front reflectors is proposed for the ITER core x-ray spectrometer. It is characterized as achieving both vertical diffraction and vertically distributed spatial viewing field with the compact front reflector set, which well fits the allocated narrow but high space in ITER equatorial port 2. The mosaic crystal HOPG is chosen for the front reflector, benefiting a good x-ray throughput and strong misalignment tolerance. XRSA simulation shows that the XRCS-Core has quite good imaging with the typical spectral resolution higher than 8000 due to the constrained aperture size in the front end.

Xe lines are selected for the XRCS-core system accompanied by an optimized combination of reflector-deflected LOSs and direct LOSs, which is thought to be applicable in various ITER scenarios with electron temperatures higher than 3 keV. The Xe⁴⁴⁺ spectrometers can provide a few available channels in low plasma parameter cases with the strongest one from the direct LOS most toward the center. In the case of a high core electron temperature (>20 keV), the XRCS-core can achieve a relatively fully viewing coverage by combining Xe⁵¹⁺ and Xe⁴⁴⁺ spectrometers. The introduction of the front reflector reduces the flexibility of the system, requiring a precise design according to the selected spectral lines. Thus, the spectral data for highly charged Xe⁵¹⁺ ions are desired for the more feasible system layout and the possibility of a prototype test.

ACKNOWLEDGMENTS

The authors would like to thank Mishra Sapna, Magesh Bharathi, and Sanjeev Varshney for the efforts in benchmarking XRSA to XICSRT, ITER SCOD staff: Loarte Alberto, Polevoi Alexei, Bonnin Xavier, and Pitts Richard for the exchange on Xe injection and transport supporting the assessment of XRCS-Core. This work was partially supported by the National Natural Science Foundation of China (Grant No. 51821005). The views and opinions expressed herein do not necessarily reflect those of the ITER Organization.

AUTHOR DECLARATIONS

Conflict of Interest

The authors have no conflicts to disclose.

Author Contributions

Zhifeng Cheng: Project administration (equal); Writing – original draft (equal). **Amro Bader:** Resources (equal); Validation

(equal). **Maarten De Bock:** Methodology (equal); Project administration (equal). **Robin Barnsley:** Conceptualization (lead). **Philippe Lorrerie:** Investigation (equal). **Novimir Pablant:** Conceptualization (equal); Methodology (equal); Software (equal); Validation (equal). **Fabio Costa:** Data curation (equal). **Joao Soeiro:** Data curation (equal). **Ines Bola:** Data curation (equal). **Martin O'Mullane:** Investigation (equal); Methodology (equal); Resources (equal). **Yevgeniy Yakusevich:** Validation (equal).

DATA AVAILABILITY

The data that support the findings of this study are available from the corresponding author upon reasonable request.

REFERENCES

- 1 A. J. H. Donné, A. E. Costley, R. Barnsley, H. Bindslev, R. Boivin, G. Conway, R. Fisher, R. Giannella, H. Hartfuss, M. G. v. Hellermann, and E. Hodgson, *Nucl. Fusion* **47**, S337 (2007).
- 2 T. Sugie, A. Costley, A. Malaquias, and C. Walker, *J. Plasma Fusion Res.* **79**, 1051–1061 (2003).
- 3 R. Barnsley, P. H. Edmonds, R. M. Giannella, and M. G. O'Mullane, in *Diagnostics for Experimental Thermonuclear Fusion Reactors 2*, edited by P. E. Stott *et al.* (Plenum Press, New York, 1998), p. 307.
- 4 R. Barnsley, M. O'Mullane, L. C. Ingesson, and A. Malaquias, *Rev. Sci. Instrum.* **75**, 3743 (2004).
- 5 M. Bitter, K. W. Hill, A. L. Roquemore, P. Beiersdorfer, S. M. Kahn, S. R. Elliott, and B. Fraenkel, *Rev. Sci. Instrum.* **70**, 292 (1999).
- 6 K. W. Hill, M. L. Bitter, S. D. Scott, A. Ince-Cushman, M. Reinke, J. E. Rice, P. Beiersdorfer, M.-F. Gu, S. G. Lee, Ch. Broennimann, and E. F. Eikenberry, *Rev. Sci. Instrum.* **79**, 10E320 (2008).
- 7 P. Beiersdorfer, J. Clementson, J. Dunn, M. F. Gu, K. Morris, Y. Podpaly, E. Wang, M. Bitter, R. Feder, K. W. Hill, and D. Johnson, *J. Phys. B: At., Mol. Opt. Phys.* **43**, 144008 (2010).
- 8 K. W. Hill, M. Bitter, L. Delgado-Aparicio, D. Johnson, R. Feder, P. Beiersdorfer, J. Dunn, K. Morris, E. Wang, M. Reinke *et al.*, *Rev. Sci. Instrum.* **81**, 10E322 (2010).
- 9 A. Serikov, U. Fischer, A. Suarez, R. Barnsley, L. Bertalot, R. O'Connor, R. Thenevin, and V. S. Udintsev, *Fusion Eng. Des.* **109–111**, 848 (2016).
- 10 H. Legall, H. Stiel, V. Arkadiev, and A. A. Bjeoumikhov, *Opt. Express* **14**, 4570 (2006).
- 11 L. F. Delgado-Aparicio, "Xe option for Ti & vt measurements in ITER," in 32nd Meeting of ITPA Topical Group on Diagnostics, Chengdu, China, 09–12 May 2017, 2017.
- 12 M. Sánchez del Río and R. J. Dejus, *Proc. SPIE* **8141**, 814115 (2011).
- 13 N. A. Pablant, A. Langenberg, J. A. Alonso, M. Bitter, S. A. Bozhenkov, O. P. Ford, K. W. Hill, J. Kring, O. Marchuck, J. Svensson, P. Traverso *et al.*, *Rev. Sci. Instrum.* **92**, 043530 (2021).
- 14 H.-K. Chung, M. H. Chen, W. L. Morgan, Y. Ralchenko, and R. W. Lee, *High Energy Density Phys.* **1**, 3 (2005).
- 15 H. Summers, ADAS User Manual, v2.6 URL <http://www.adas.ac.uk/manual.php>, 2004.
- 16 R. Dux, A. Loarte, E. Fable, and A. Kukushkin, *Plasma Phys. Control. Fusion* **56**, 124003 (2014).
- 17 R. Dux, A. G. Peeters, A. Gude, A. Kallenbach, R. Neu, and A. U. Team, *Nucl. Fusion* **39**, 1509 (1999).
- 18 A. R. Polevoi, A. Loarte, R. Dux, T. Eich, E. Fable, D. Coster, S. Maruyama, S. Y. Medvedev, F. Köchl, and V. E. Zhogolev, *Nucl. Fusion* **58**, 056020 (2018).
- 19 J. E. Rice, K. B. Fournier, G. E. Kemp, M. Bitter, N. Cao, L. Delgado-Aparicio, K. Hill, A. E. Hubbard, J. W. Hughes, and M. L. Reinke, *J. Phys. B: At., Mol. Opt. Phys.* **53**, 055701 (2020).
- 20 P. Beiersdorfer, S. Von Goeler, M. Bitter, E. Hinnov, R. Bell, S. Bernabei, J. Felt, K. W. Hill, R. Hulse, J. Stevens, and S. Suckewer, *Phys. Rev. A* **37**, 4153 (1988).